

GLIMPSE: Generalized Local Imaging with MLPs

AmirEhsan Khorashadizadeh, Valentin Debarnot, Tianlin Liu, and Ivan Dokmanić

Abstract—Deep learning is the current de facto state of the art in tomographic imaging. A common approach is to feed the result of a simple inversion, for example the backprojection, to a convolutional neural network (CNN) which then computes the reconstruction. Despite strong results on “in-distribution” test data similar to the training data, backprojection from sparse-view data delocalizes singularities, so these approaches require a large receptive field to perform well. As a consequence, they overfit to certain global structures which leads to poor generalization on out-of-distribution (OOD) samples. Moreover, their memory complexity and training time scale unfavorably with image resolution, making them impractical for application at realistic clinical resolutions, especially in 3D: a standard U-Net requires a substantial 140GB of memory and 2600 seconds per epoch on a research-grade GPU when training on 1024×1024 images. In this paper, we introduce GLIMPSE, a *local* processing neural network for computed tomography which reconstructs a pixel value by feeding only the measurements associated with the neighborhood of the pixel to a simple MLP. While achieving comparable or better performance with successful CNNs like the U-Net on in-distribution test data, GLIMPSE significantly outperforms them on OOD samples while maintaining a memory footprint almost independent of image resolution; 5GB memory suffices to train on 1024×1024 images. Further, we built GLIMPSE to be fully differentiable, which enables feats such as recovery of accurate projection angles if they are out of calibration.

Index Terms—Deep Learning, Computed Tomography, MLP, Uncalibrated Imaging

I. INTRODUCTION

CONVOLUTIONAL neural networks (CNNs) have become the standard approach for tomographic image reconstruction where the goal is to recover the image from noisy (non-)linear measurements [1]. U-Net [2] has emerged as the architecture underpinning the majority of deep learning reconstruction methods, applied with great success to a variety of imaging problems including computed tomography (CT) [3], magnetic resonance imaging (MRI) [4] and photoacoustic tomography [5]. Its success is often attributed to its multi-scale architecture [6].

At the same time, certain aspects of multi-scale CNNs complicate their application to real problems. Despite satisfactory results on in-distribution test images similar to the training

This project was supported by the European Research Council Starting under Grant 852821—SWING.

AmirEhsan Khorashadizadeh, Valentin Debarnot and Tianlin Liu are with the Department of Mathematics and Computer Science of the University of Basel, 4001 Basel, Switzerland (e-mails: amir.kh@unibas.ch, valentin.debarnot@unibas.ch, t.liu@unibas.ch).

Ivan Dokmanić is with the Department of Mathematics and Computer Science of the University of Basel, 4001 Basel, Switzerland, and also with the Department of Electrical, Computer Engineering, the University of Illinois at Urbana-Champaign, Urbana, IL 61801 USA (e-mail: ivan.dokmanic@unibas.ch).

Our implementation is available at <https://github.com/swing-research/Glimpse>

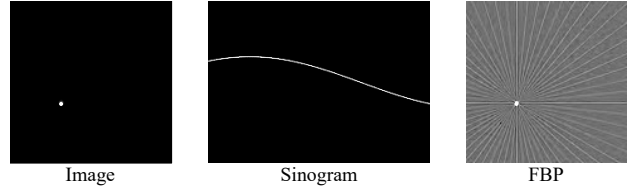


Fig. 1: A point source image, its sinogram, and the sparse view FBP reconstruction; while the corresponding measurements for this pixel have sinusoidal support in the sinogram, this information is diffused along the FBP image. We stretched the contrast of the FBP image for a better visualization.

data, they often overfit specific image content resulting in poor generalization on out-of-distribution changes in image content and sensor shifts. Model-based networks struggle to address this drawback by integrating the forward and adjoint operators into multiple network layers or iterations [7]–[12]. However, the required memory for CNNs directly scales with image resolution [13]. For instance, the widely used U-Net requires a substantial 140GB memory and 2600 seconds per epoch when training on 1024×1024 images using two Tesla A100 GPUs. This latter drawback is further exacerbated with model-based networks like learned primal-dual reconstruction (LPD) [8] which achieves strong performance but requires over 80GB memory even at a lower resolution 512×512 . This increased memory demand is due to the repeated application of the forward model and its adjoint in forward and backward passes of the neural network. This makes standard CNN-based pipelines impractical for real-world scenarios involving resolutions beyond 512×512 or 3D problems.

To better understand the mechanics behind the poor generalization of U-Net-like CNNs which compute the reconstruction from filtered backprojections (FBP) [14], we designed an experiment as follows. Figure 1 shows an object with a point source, its sparse view sinogram measurements with sinusoidal support, and the FBP reconstruction supported over the entire field of view. This observation raises the question of the ideal receptive field size for CNNs like U-Net, as they would seemingly require a deep network with a large receptive field to cover all the information distributed across the FBP image in the input [15], [16].

However, models with large receptive fields often overfit the specific image content in training data leading to poor generalization on out-of-distribution samples. Indeed, Figure 2 shows that while the U-Net produces good results when tested on in-distribution data similar to training data (here chest images), it performs poorly on out-of-distribution (OOD) brain images. This is primarily due to the large receptive field which causes overfitting to global features. This limitation makes CNNs

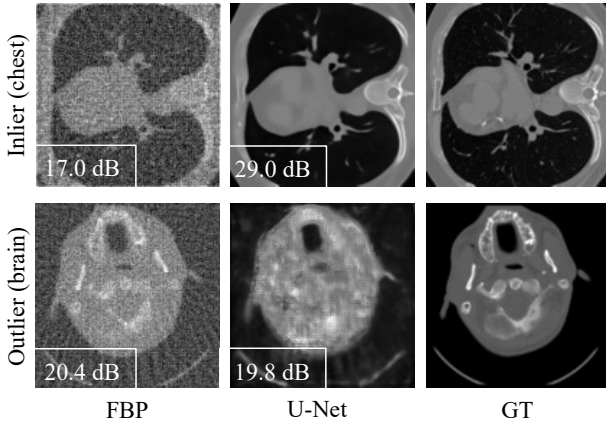


Fig. 2: Performance of U-Net [2] trained on chest images: evaluation on in-distribution test data (chest samples) and OOD brain samples shows that the large receptive field of the U-Net hinders its ability to generalize on OOD samples, with its PSNR even falling below that of FBP reconstruction.

like U-Net inappropriate for real-world applications, especially in domains such as medical imaging where robustness over distribution shifts and other uncertain and variable factors is paramount [17].

In this paper, we introduce a new deep learning imaging architecture termed GLIMPSE—a local processing neural network with a simple design adapted to the geometry of computed tomography. As shown in Figure 3, to recover the image intensity at a given target pixel, we use a multi-layer perceptron (MLP) that takes only the local sinogram measurements associated with this pixel and its neighbors. In contrast to CNNs like the U-Net, which globally process the input at once, GLIMPSE allows the MLP to focus exclusively on the *local neighborhood* of the sine curve. This localization results in robust performance, particularly when dealing with OOD data.

At the same time, this design makes GLIMPSE highly computationally efficient; it permits training on mini-batches of both *pixels* and objects. This flexibility leads to fast and efficient training, requiring a small, fixed amount of memory almost *independent* from the image resolution. This allows training GLIMPSE on large, realistic images like in resolution 1024×1024 .

We built GLIMPSE to be fully differentiable, all the way down to the sensing and integration geometry. This differentiable framework presents several advantages over the standard CNN-based architectures. For instance, most methods for CT image recovery strongly rely on the sensor geometry information encoded in the forward operator, whether explicitly, as seen in methods like FBP [14], SART [18], LGS [7], and LPD [8] or implicitly as used in U-Net [2] when taking FBP as input. This fixed geometry is a problem when faced with uncertainties in calibration or blind inversion problems where the sensor geometry information is entirely unavailable. While such uncertainties might substantially degrade the quality of reconstructions of the standard methods [19], [20], our fully differentiable architecture allows the optimization of projec-

tion angles during training, which yields both an accurate estimation of the actual sensor geometry from data and high-quality reconstructions even in the presence of substantial noise in measurements and the absence of any prior information regarding sensor positions.

II. RELATED WORK

Model-based vs Model-free Inversion. There are two major classes of deep-learning-based approaches to CT: *model-based* and *model-free* inversion. In the model-based approach, neural networks process raw sinograms and map them to the desired CT images while the Radon transform is integrated into multiple network layers or iterations [7], [8], [11]. These methods perform remarkably well across various inverse problems, but they are computationally expensive, especially during training [13]. The high computational cost is due, among other factors, to the repeated application of the Radon transform and its adjoint in forward and backward passes of the neural networks.

In contrast, model-free approaches offer a computationally cheaper alternative. The Radon transform (or its adjoint) is only used once in FBP computation before the neural network [3], [21], [22]. However, these models often require deep networks with a large receptive field to leverage the information delocalized across the FBP image. Recently, Hamoud et al. [16] used a measurement rearrangement technique to stratify backprojected features by angle and thus enable the use of smaller, shallower CNNs.

Uncalibrated CT Imaging. In CT imaging, the acquisition operator is often known but obtains insufficient measurements. This may occur when a reduced number of projections is used to minimize radiation exposure or shorten acquisition time (sparse view) or when only a limited cone of projection angles may be used (limited view). In certain situations, the acquisition operator is only partially known due to uncertain experimental conditions giving rise to uncalibrated imaging or blind inversion. Neglecting this uncertainty can result in a significant drop in the quality of the reconstructions [19]. To tackle this challenge, total least squares approaches have been developed, involving the perturbation of an assumed forward operator [23]–[25]. Recently, Gupta et al. [20] used autodifferentiation and gradient descent to estimate the uncalibrated forward operator in a self-consistent manner.

MLPs for Patches. A Multi-layer perceptron (MLP) is a fundamental neural network architecture used in a great variety of applications. Recently, vision transformers [26] and MLP-mixers [27] have shown promising performance in various computer vision tasks like image classification [28] and image restoration [29]. While a vanilla MLP lacks a good inductive bias for imaging, in particular translation equivariance—very much unlike CNNs—vision transformers and MLP-mixers restore it by processing patches instead of entire images [30]. However, these strategies require large datasets and networks to achieve performance comparable with CNNs. In our work, we leverage the patch-based inductive bias [31], [32] in the context of CT imaging, demonstrating that even a small MLP can achieve performance on par with or even surpassing that of popular image-to-image CNNs.

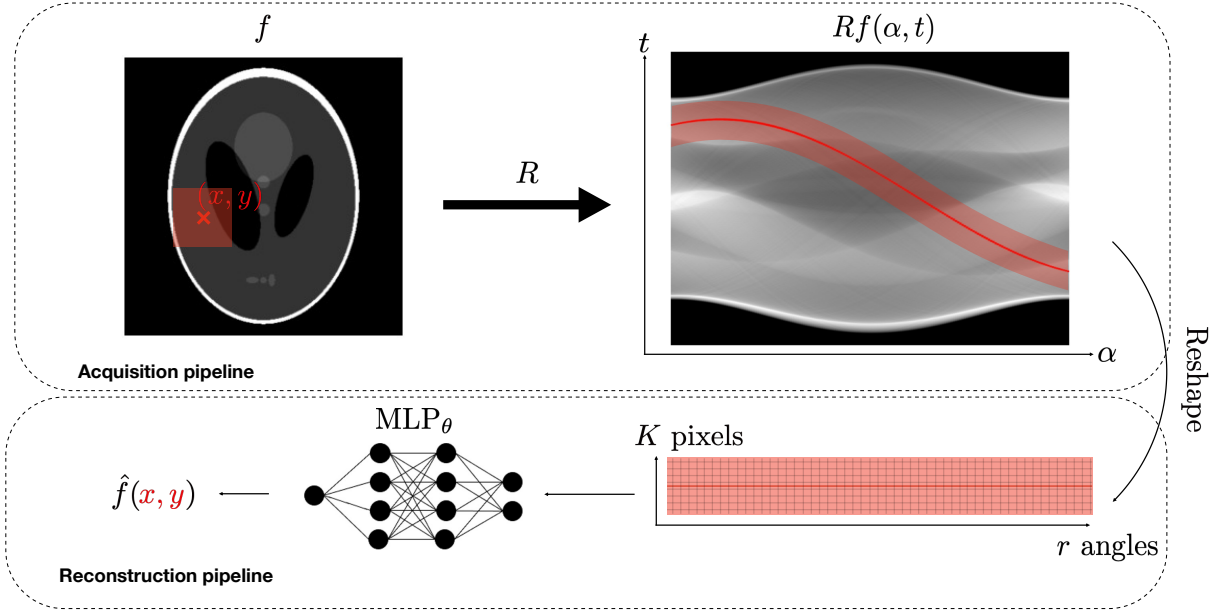


Fig. 3: GLIMPSE; a small MLP processes the measurements associated with the pixel (x, y) and its neighbors extracted from the sinogram. This local processing network has promising performance on OOD data while being computationally efficient all due to its patch-based design.

III. COMPUTED TOMOGRAPHY

CT imaging [33] plays an important role in many applications including medical diagnosis [34], industrial testing [35], and security [36]. We consider 2D computed tomography where the image of interest $f(\mathbf{x})$ with size $D \times D$ is reconstructed from the measurements of wave attenuation where $\mathbf{x} = (x, y) \in \mathbb{R}^2$ denotes the coordinate. The forward model is the Radon transform Rf which computes integrals of $f(\mathbf{x})$ along lines L ,

$$Rf(L) = \int_L f(\mathbf{x}) |d\mathbf{x}|. \quad (1)$$

We parameterize a line L by its distance from the origin t and its normal vector's angle with the X -axis α . We can then reformulate (1) as

$$Rf(\alpha, t) = \int_{-\infty}^{\infty} f(x(z), y(z)) dz, \quad (2)$$

where,

$$x(z) = z \cos(\alpha) - t \sin(\alpha), \quad (3)$$

$$y(z) = z \sin(\alpha) + t \cos(\alpha). \quad (4)$$

The image of interest is observed from a finite set of r different viewing directions $\{\alpha_m\}_{m=1}^r$, each having N parallel, equispaced rays. The measurements of the attenuation are then represented as a transform-domain “image” $\mathbf{s} \in \mathbb{R}^{N \times r}$ called a sinogram.

Standard methods for CT image recovery discretize the image of interest $f(\mathbf{x})$ into a discrete image $\mathbf{f} \in \mathbb{R}^{N \times N}$

supported on an $N \times N$ grid. After discretization, the forward model can be written as

$$\mathbf{s} = \mathbf{A}\mathbf{f} + \mathbf{n}. \quad (5)$$

where \mathbf{A} denotes the discretized Radon transform and we model the measurement noise by \mathbf{n} . The most commonly used analytical inversion method is the filtered backprojection (FBP),

$$\mathbf{f}_{x,y}^{\text{FBP}} = \sum_{m=1}^r \tilde{\mathbf{s}}[y \cos(\alpha_m) - x \sin(\alpha_m), m], \quad (6)$$

where $\mathbf{f}_{x,y}^{\text{FBP}} \in \mathbb{R}^{N \times N}$ is the FBP reconstruction, $\tilde{\mathbf{s}}[\cdot, m] = \mathbf{s}[\cdot, m] * \mathbf{h}$, \mathbf{h} is a certain high-pass filter, $*$ denotes the convolution and linear interpolation is used in (6) for evaluating $\tilde{\mathbf{s}}[x, \cdot]$ when x is not an integer. As shown in Proposition 2 in Section S-2 in the supplementary information, while the Ram-Lak filter is the optimal choice for \mathbf{h} in the case of noise-free complete measurements, it can amplify the noise in real-world noisy measurements, leading to poor reconstruction.

With measurement noise and an incomplete collection of projections, tomographic image reconstruction from a sinogram becomes an ill-posed inverse problem that requires an image prior. In the following section, we introduce our proposed method, GLIMPSE, designed so that it respects the geometry of CT imaging.

A. GLIMPSE: Local Imaging with MLPs

To recover the image $\mathbf{f}(x, y)$ at pixel (x, y) , we identify the elements in the sinogram \mathbf{s} influenced by this pixel. As illustrated in Figure 1, the corresponding measurements for

the pixel (x, y) are supported along a sinusoidal curve in the sinogram; we denote them $\text{SIN}_{x,y} \in \mathbb{R}^r$, with elements being given as

$$\text{SIN}_{x,y}[m] = \mathbf{s}[y \cos(\alpha_m) - x \sin(\alpha_m), m]. \quad (7)$$

Similar to (6), we can use interpolation to evaluate $\mathbf{s}[x, \cdot]$ for non-integer x . This localization is formally captured by the following proposition.

Proposition 1 (Impulse response of Radon transform). *Let $f(u, v) = \delta(u - x, v - y)$ be the Dirac delta distribution in \mathbb{R}^2 at location (x, y) . Its Radon transform (in the sense of distributions) is*

$$Rf(\alpha, t) = \begin{cases} 1, & \text{if } t = y \cos(\alpha) - x \sin(\alpha) \\ 0, & \text{otherwise.} \end{cases}$$

The proof is standard and given for completeness in Section S-3 in the supplementary information.

The sinusoidal portion of the (filtered) sinogram $\text{SIN}_{x,y}$ should have enough information to recover the pixel intensity (x, y) as it contains all the measurements associated with this pixel. However, because the projections are corrupted with noise and only come from a subset of all possible projection angles, incorporating ‘‘contextual information’’ about the target pixel improves reconstruction quality. As shown in Figure 3, we exploit the spatial regularity of medical images (encoded in training data) by using the measurements which provide *local* information around (x, y) . This ensures that the model does not overfit large-scale features in the training data while maintaining low computational complexity. We thus additionally extract from the sinogram the regions associated with the neighboring pixels around (x, y) and store this information in vector $\mathbf{p}_{x,y}$,

$$\mathbf{p}_{x,y} = \{\text{SIN}_{x+dn, y+dn'} | n, n' = -\lfloor C/2 \rfloor, \dots, \lfloor C/2 \rfloor\}, \quad (8)$$

where $K = C^2$ determines the number of neighboring pixels around (x, y) for an odd number $C \geq 1$ and d denotes the scale of the window which adjusts the receptive field. We concatenate the vectors inside $\mathbf{p}_{x,y}$ and make a long vector $\mathbf{p}_{x,y} \in \mathbb{R}^{r \times K}$. In order to recover the image at pixel (x, y) from $\mathbf{p}_{x,y}$, we use a multi-layer perception $\text{MLP}_\theta : \mathbb{R}^{r \times K} \rightarrow \mathbb{R}$ parameterized by θ ,

$$\hat{\mathbf{f}}_{x,y} = \text{MLP}_\theta[\mathbf{p}_{x,y}], \quad (9)$$

which approximates the pixel intensity $\hat{\mathbf{f}}_{x,y}$ from the local features around (x, y) . We call the proposed model GLIMPSE. In the following section, we describe how our implementation of GLIMPSE allows to compensate for calibration errors as well as to adapt to noisy measurements. We then propose a training strategy with resolution-agnostic memory usage in Section III-D. Further details for network architecture and training can be found in Section S-1 in supplementary information.

B. Learned Sensor Geometry

The knowledge of projection angles $\{\alpha_m\}_{m=1}^r$ is a fundamental prerequisite in most CT image recovery algorithms, for example in FBP [14], SART [18], LGS [7], LPD [8]. Consequently, in an uncalibrated system where access to accurate sensor geometry information is lacking, the quality of reconstruction may suffer [19], [37]. To address this challenge, our top-down differentiable framework, GLIMPSE, allows optimizing the projection angles to retrieve $\{\alpha_m\}_{m=1}^r$ during training, see Section III-D. As we will show in experiments, GLIMPSE can accurately estimate the actual projection angles $\{\alpha_m\}_{m=1}^r$ purely from data resulting in high-quality reconstructions comparable with those achieved in an ideal calibrated system while maintaining strong OOD performance, unlike methods that do not attempt to correct the projection angles. As we jointly optimize $\{\alpha_m\}_{m=1}^r$ with other trainable parameters using end-to-end training, this additional angle estimation incurs a very modest computational cost. We refer to the model incorporating the learned sensor geometry as GLIMPSE (LSG), distinguishing it from the vanilla version, GLIMPSE (vanilla), which assumes a fixed sensor geometry.

C. Adaptive Filtering for Noisy Measurements

As shown in Section S-2 in the supplementary information, the Ram–Lak high-pass filter is the optimal filter \mathbf{h} for the FBP reconstruction in the case of complete noise-free measurements. In real applications, however, we always encounter noisy projections from a subset of angles. The Ram–Lak filter is then suboptimal and typically degrades the reconstruction quality as it amplifies high-frequency noise. Alternative filters with lower amplitudes in high frequencies like Shepp–Logan, cosine, and Hamming have been used to mitigate the noisy measurements, but they are all ad hoc choices. It would be better to adapt \mathbf{h} to the specifics of noise and sampling strategy in the target application. To design this task-specific filter, we let MLP_θ take as input the filtered sinogram $\tilde{\mathbf{s}}[\cdot, m] = \mathbf{s}[\cdot, m] * \mathbf{h}$ and consider the filter \mathbf{h} (in Fourier space) as trainable parameters to be optimized during training. This allows us to automatically learn a noise-adaptive filter from data, again with almost no additional computational cost.

D. Resolution-agnostic Memory Usage in Training

To simplify notation, we denote the entire GLIMPSE pipeline described above by $\hat{\mathbf{f}} = \text{GLIMPSE}_\phi(\mathbf{x}, \mathbf{s})$. The inputs are the target pixel coordinates $\mathbf{x} = (x, y)$ and the sinogram \mathbf{s} ; the output is an estimate of $\mathbf{f}(x, y)$. The parameters ϕ denote the trainable parameters of GLIMPSE including the MLP weights θ , the projection angles $\{\alpha_m\}_{m=1}^r$, the adaptive filter \mathbf{h} and the patch receptive field scale d . We consider a set of training data $\{(\mathbf{s}_i, \mathbf{f}_i)\}_{i=1}^L$ from the noisy sinograms and images. We optimize the GLIMPSE parameters ϕ using gradient-based optimization to minimize

$$\phi^* = \underset{\phi}{\operatorname{argmin}} \sum_{i=1}^{N^2} \sum_{j=1}^L |\text{GLIMPSE}_\phi(\mathbf{x}_i, \mathbf{s}_j) - \mathbf{f}_j(\mathbf{x}_i)|^2. \quad (10)$$

At inference time, we simply evaluate the image intensity at any pixel as $\hat{\mathbf{f}}_{\text{test}}(\mathbf{x}) = \text{GLIMPSE}_{\phi^*}(\mathbf{x}, \mathbf{s}_{\text{test}})$. One major advantage of GLIMPSE compared to CNNs like the U-Net and LPD is its memory and compute complexity. CNN-based models exhibit memory requirements that scale directly with image resolution, making them prohibitively expensive for realistic image resolutions. As shown in (10), GLIMPSE can be trained using stochastic gradient-based optimizers with the flexibility to select mini-batches from both the objects and *pixels*. This adaptability in mini-batch pixel selection grants a memory footprint agnostic to resolution making GLIMPSE suitable for training on realistic image resolutions like 1024×1024 and higher.

IV. EXPERIMENTS

We simulate parallel-beam X-ray CT with $r = 30$ projections uniformly distributed around the object. We consider 30dB measurement noise. The reconstruction quality is quantified using the peak signal-to-noise ratio (PSNR) and Structural Similarity Index (SSIM) [38]. We compare the performance of GLIMPSE with successful CNN-based models: the U-Net [2], learned gradient scheme (LGS) [7] and learned primal-dual (LPD) [8] for sparse view CT image reconstruction. We use 35820 training samples of chest images from the LoDoPaB-CT dataset [39] in resolution 128×128 . Model performance is assessed on 64 in-distribution test samples of chest images, while 16 OOD brain images [40] are included to evaluate the generalization capability of the models. For further information regarding the network architectures and training details please refer to Section S-1.

In Section IV-A, we conduct a comparative analysis of GLIMPSE against CNN-based models for sparse view CT image reconstruction on both in-distribution and OOD data. In Section IV-B, we analyze the computational efficiency of the aforementioned models. Section IV-C addresses the uncalibrated and blind scenarios. We analyze the learned filters \mathbf{h} across different measurement noise levels in Section IV-D. Finally in Section IV-E, we study performance of GLIMPSE for different patch sizes.

A. Sparse view CT Image Reconstruction

The upper row of Figure 4 and Table Ia show the performance of different models on in-distribution test samples of chest images. This experiment shows that GLIMPSE, by leveraging only a single MLP network, can outperform successful CNNs like U-Net and achieve comparable performance with state-of-the-art LGS and LPD methods.

The lower row of Figure 4 and Table Ia provide a comparative analysis of the performance of various models trained on chest images when applied to OOD brain images. This experiment demonstrates that while U-Net excels on in-distribution samples, its performance significantly deteriorates on OOD data. This decline in performance may be attributed to the U-Net’s large receptive field which results in overfitting to large-scale features. We emphasize that this large receptive field is important to capture information delocalized in the filtered backprojection image and achieve strong performance.

TABLE I: Comparative analysis of different models for sparse view CT image reconstruction

(a) The reconstruction quality averaged on 64 test samples

	In-distribution (chest)		Out-of-distribution (brain)	
	PSNR	SSIM	PSNR	SSIM
FBP [14]	17.0	0.17	17.1	0.22
U-Net [2]	30.1	0.84	15.1	0.28
LGS [7]	30.9	0.84	20.5	0.54
LPD [8]	31.6	0.86	25.5	0.76
GLIMPSE	30.9	0.84	25.1	0.79

(b) Memory usage and training time

	GLIMPSE	U-Net [2]	LGS [7]	LPD [8]
Num params	900k	7800k	19k	400k
128×128	4GB / 114s	6GB / 34s	4GB / 384s	13GB / 963s
256×256	4GB / 123s	16GB / 117s	13GB / 575s	41GB / 1517s
512×512	4GB / 185s	53GB / 460s	45GB / 1682s	> 80GB
1024×1024	5GB / 419s	> 80GB	> 80GB	> 80GB

Indeed, reducing the receptive field, while a potential remedy for poor generalization on OOD data, may compromise the reconstruction quality even on in-distribution test data.

On the contrary, GLIMPSE demonstrates remarkable performance on OOD data. Although LPD’s performance on OOD data is sometimes comparable or slightly better than that of GLIMPSE, it comes at a very high memory and compute cost due to the repeated application of the forward operator and its adjoint in the network architecture.

B. Computational Efficiency

The fact that LPD far outperforms the U-Net on OOD data is a testament to the benefits of incorporating the forward operator in the architecture. On the other hand, as evident from Table Ib, it comes at a cost of unfavorable training time and memory footprint which rapidly worsens with resolution. Table Ib shows that CNN-based models may become impractical already at resolutions like 512×512 , even on GPUs with 80GB memory.

On the other hand, GLIMPSE is computationally efficient; the memory usage remains almost unaffected by image resolution. Remarkably, GLIMPSE can be trained with only 5GB memory in less than a day, even when dealing with resolutions of 1024×1024 and higher. Figure 5 shows the performance of GLIMPSE on in-distribution and OOD samples in resolution 512×512 where we considered 40dB measurement noise. This experiment demonstrates that even a small MLP can achieve reconstructions with near state-of-the-art quality in realistic high resolutions while maintaining a rather modest memory footprint.

C. Uncalibrated Imaging and Blind Inversion

In this section, we assess the performance of GLIMPSE in situations with calibration mismatch. In the following experiments, we place $r = 30$ sensors uniformly around the object at angles $\alpha = 0^\circ, 6^\circ, \dots, 174^\circ$. We conduct a comparative analysis of three models: 1) GLIMPSE (vanilla),

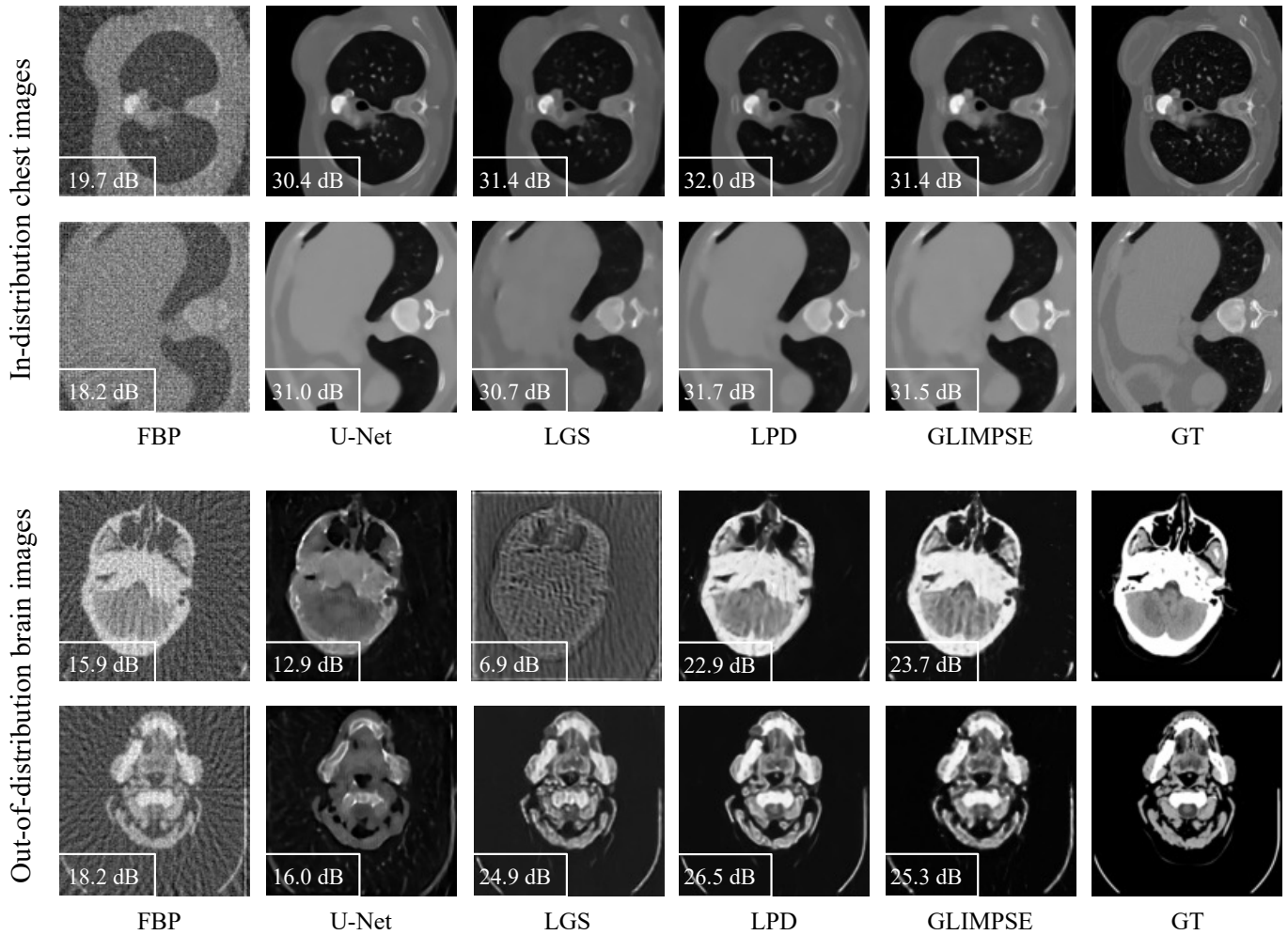


Fig. 4: Performance of different models trained on training data of chest images evaluated on in-distribution and OOD samples for sparse view CT image reconstruction. GLIMPSE has excellent performance on OOD data due to its localized MLP, significantly better than U-Net [2] and LGS [7] and comparable with LPD [8].

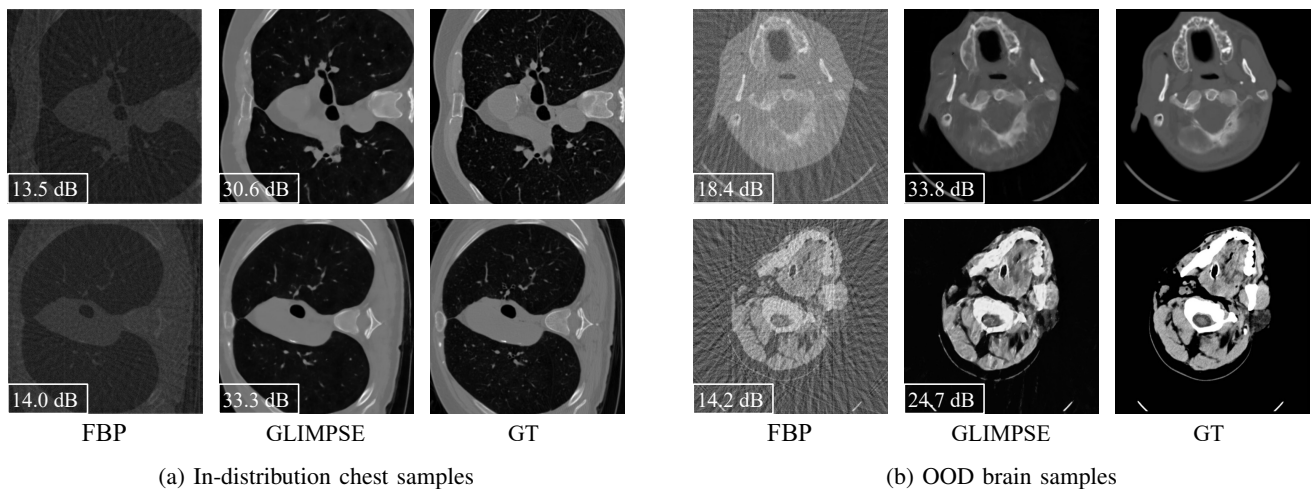


Fig. 5: GLIMPSE's performance in resolution 512×512 trained on chest training data with $r = 30$ projections and 40dB noise; GLIMPSE requires only 4GB memory and can be trained in less than 10 hours on a single GPU.

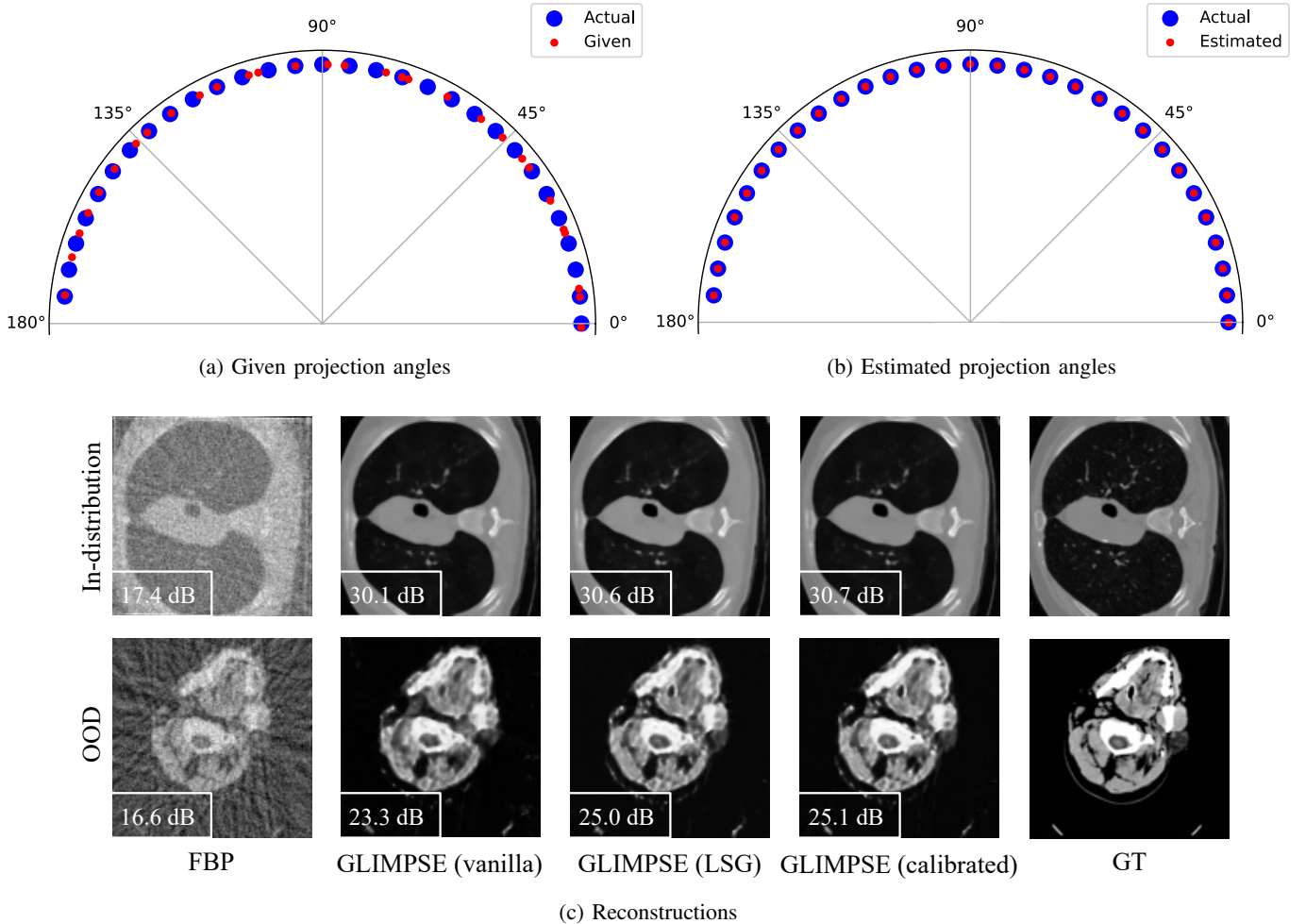


Fig. 6: Estimated sensor geometry by GLIMPSE (LSG) and reconstructions for an uncalibrated system with a random sensor shift; as expected, the learnable sensor geometry can effectively learn the projection angles and exhibits excellent robustness with no degradation under such a big model mismatch and measurement noise (30dB).

featuring no learnable sensor geometry, 2) GLIMPSE (LSG), incorporating the proposed learned sensor geometry outlined in Section III-B, and 3) GLIMPSE (calibrated), operating under ideal conditions with no model mismatch (informed with correct projection angles). We let the GLIMPSE (LSG) learn the projection angles from the training data where the optimized values $\{\alpha_m\}_{i=1}^r$ obtained through training can provide a reliable estimate of the actual projection angles.

Uncalibrated system with random sensor shifts: As shown in Figure 6a, we randomly perturb projection angles by a normally distributed error so that $\alpha_i^{\text{given}} = \mathcal{N}(\alpha_i, \sigma^2)$; we set $\sigma = 2^\circ$. Figure 6b shows the estimated angles obtained through training—GLIMPSE (LSG) accurately recovers the angles with 30dB measurement noise. As shown in Figure 6c, this accurate estimation of projection angles results in high-quality reconstructions by GLIMPSE (LSG) comparable with the network trained in an ideal calibrated system.

Uncalibrated system with fixed sensor shifts: As depicted in Figure 7a, we consider an uncalibrated system where the provided information about the projection angles deviates by 3° from the actual positions, namely, $\alpha_i^{\text{given}} = \alpha_i + 3^\circ$. As

depicted in Figure 7b, the estimated projection angles by the GLIMPSE (LSG) showcase its capability to accurately recover sensor positions from the training data. Figure 7c demonstrates the reconstructions for in-distribution and OOD data. This experiment shows that the performance of GLIMPSE (vanilla) sharply dropped in this uncalibrated system, particularly on OOD data. While its MLP module attempts to compensate for the model mismatch and succeeds to some extent on in-distribution chest images, this compensation comes at the cost of overfitting the training data, resulting in poor generalization to OOD samples. This experiment showcases GLIMPSE (LSG) as a robust deep learning model under model mismatch, well-suited for handling real-world challenges.

Blind inversion with no information from projection angles: We consider the blind scenario where the model operates without any prior knowledge of the sensor geometry making inversion challenging. As shown in Figure 8a, we inevitably initialize the projection angles $\{\alpha_m\}_{i=1}^r$ in the GLIMPSE (LSG) architecture with random values.

The estimated projection angles are shown in Figure 8b, highlighting GLIMPSE (LSG)’s impressive ability for data-

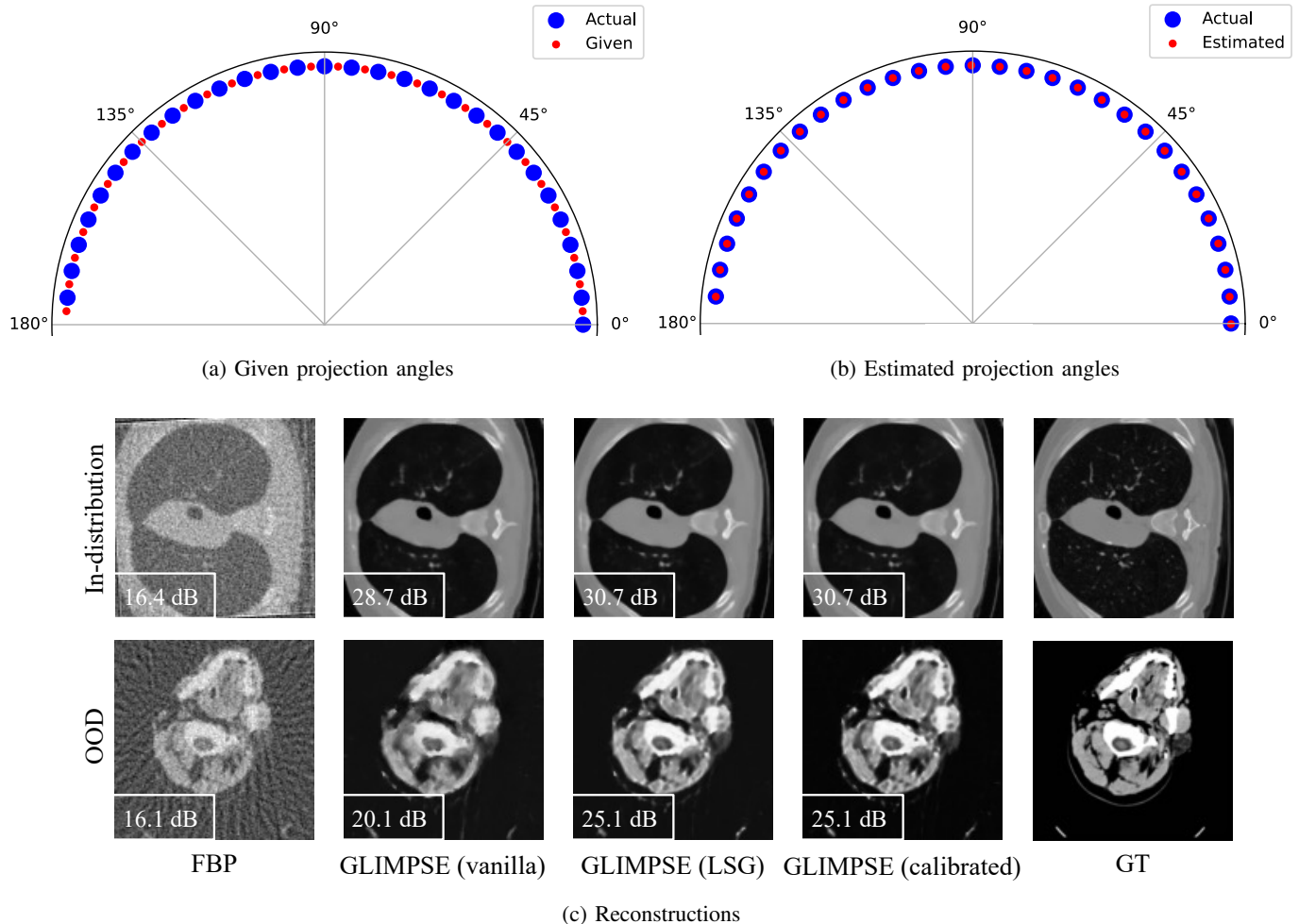


Fig. 7: Estimated sensor geometry by GLIMPSE (LSG) and reconstructions for an uncalibrated system with a fixed 3° sensor shift; as expected, the learnable sensor geometry can effectively learn the projection angles and exhibits excellent robustness.

driven sensor geometry estimation. Figure 8c presents the reconstructions achieved by GLIMPSE in both its vanilla and LSG versions. As expected, FBP and the GLIMPSE (vanilla) show poor reconstructions due to the missing sensor geometry information. On the other hand, GLIMPSE (LSG) could accurately reconstruct both in-distribution and OOD samples. Remarkably, these results are comparable to those achieved by the calibrated GLIMPSE with informed projection angles. Table II provides quantitative results averaged on 64 test samples.

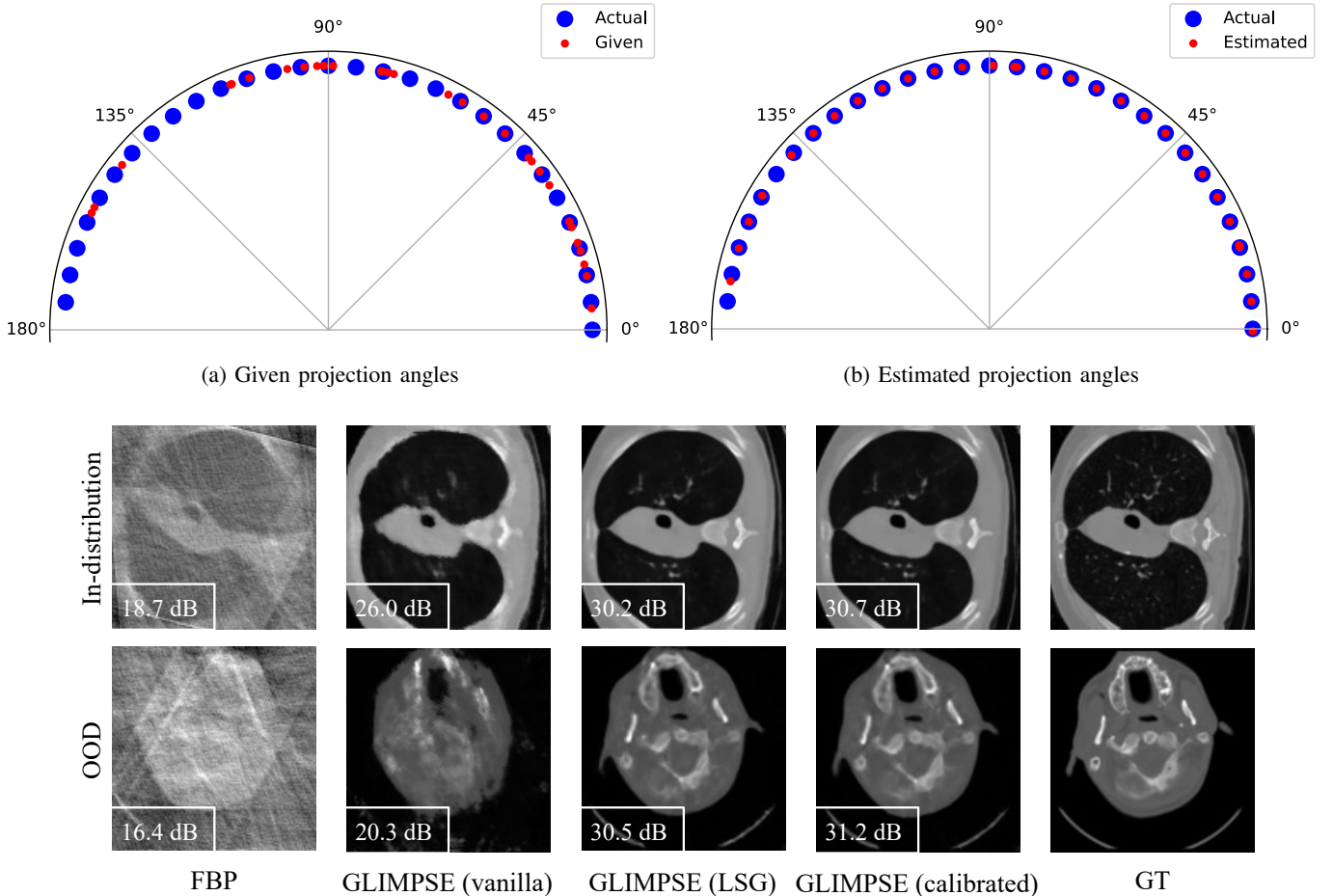
D. Learned Filter

In this section, we analyze the behavior of the learned filter obtained through training of GLIMPSE introduced in section III-C across datasets with different measurement noise levels. This analysis provides useful signal processing insights into how the properties of the learned filter are influenced by varying noise levels. The frequency response of the learned filters is depicted in Figure 9, alongside well-known hand-crafted filters such as Ram-Lak, Shepp-Logan, and hamming filters. These learned filters are derived from GLIMPSE training on datasets characterized by different noise levels.

TABLE II: Model performance in PSNR (dB) averaged on 64 test samples for models with different levels of sensor geometry information: 1) calibrated, complete information 2) uncalibrated, with fixed and random sensor shifts 3) blind, no information.

(a) In-distribution chest samples			
	FBP	GLIMPSE (vanilla)	GLIMPSE (LSG)
Calibrated (complete info)	17.0	30.9	30.9
Uncalibrated (fixed shifts)	15.9	30.1	30.9
Uncalibrated (random shifts)	16.9	30.6	30.9
Blind (No info)	12.4	26.7	30.5

(b) OOD brain samples			
	FBP	GLIMPSE (vanilla)	GLIMPSE (LSG)
Calibrated (complete info)	17.1	25.1	25.1
Uncalibrated (fixed shifts)	15.6	20.0	25.1
Uncalibrated (random shifts)	16.1	23.2	25.0
Blind (No info)	10.8	14.9	24.1



(c) High-quality reconstructions by GLIMPSE (LSG) despite having no information from sensor geometry.

Fig. 8: Estimated sensor geometry by GLIMPSE (LSG) and reconstructions for blind inversion; GLIMPSE (LSG) was initialized with random projection angles $\{\alpha_m\}_{i=1}^r$ (a) could reliably estimate the projection angles purely from data (b) resulting in high-quality reconstructions (c).

As expected and discussed in Section S-2, the learned filter for noise-free measurements exhibits behaviors akin to the Ram-Lak filter, displaying high values in high frequencies. Intriguingly, as the noise level increases (by decreasing the noise SNR), the filter progressively takes smaller values in high frequencies to suppress the noise. This experiment demonstrates that GLIMPSE is capable of autonomously adapting the characteristics of the filter according to the noise level observed in the training data. Reconstructed images for different noise levels are presented in Figure 10.

E. Ablation Study on Patch Size

In this section, we investigate the impact of varying the number of neighboring pixels $K = C^2$, on the GLIMPSE’s performance. Table III shows the performance of GLIMPSE trained with different numbers of neighboring pixels K on in-distribution and OOD samples. The table demonstrates that the reconstruction quality tends to reach a saturation point beyond a certain patch size. This observation provides insights into understanding the upper limit of local information crucial for accurate reconstructions.

TABLE III: Reconstruction quality in PSNR (dB) for GLIMPSE trained with various window sizes

Patch size ($K = C^2$)	In-distribution	OOD	Num params
1×1	25.6	18.3	280k
3×3	30.2	24.2	345k
5×5	30.7	24.9	470k
7×7	30.8	24.9	650k
9×9	30.9	25.1	900k
11×11	30.9	25.0	1200k

V. LIMITATIONS AND CONCLUSION

In this paper, we use the natural notion of locality for CT image reconstruction, moving away from CNNs that reconstruct the image as a whole. Our approach adopts a coordinate-based strategy, focusing on processing the sinusoidal curves in the sinogram associated with each pixel using a small MLP. Our results demonstrate that this localized processing framework exhibits robust performance on OOD data while maintaining nearly constant memory requirements across different resolutions; thereby being computationally efficient even at realistic

REFERENCES

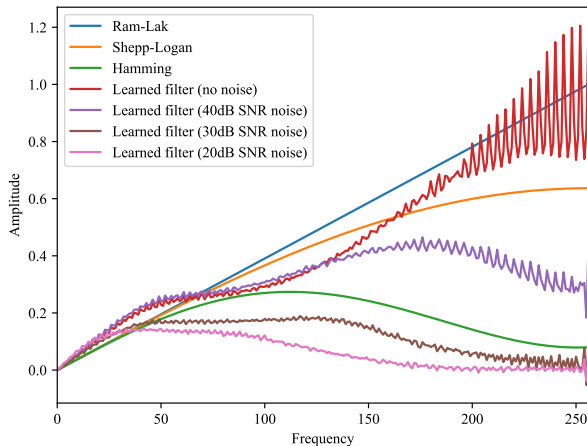


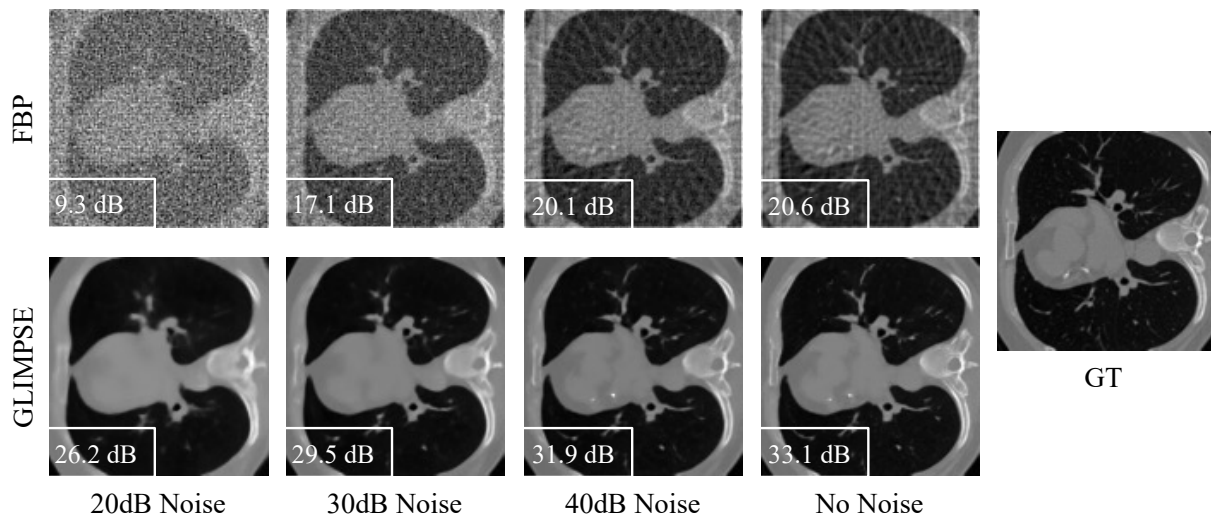
Fig. 9: The learned filter for datasets with different noise levels, all the filtered are initialized by Ram-Lak filter in GLIMPSE architecture. By increasing the noise level, the filter assigns smaller amplitudes for high-frequencies to suppress the noise and aligns with the optimality of the Ram-Lak filter for noise-free complete measurements shown in Section S-2.

high resolutions. Furthermore, our fully differentiable architecture presents versatility in addressing real-world challenges in medical imaging. Specifically, we showed its applicability in learning sensor geometry for uncalibrated systems and adapting the learned filter according to the noise level observed in training data.

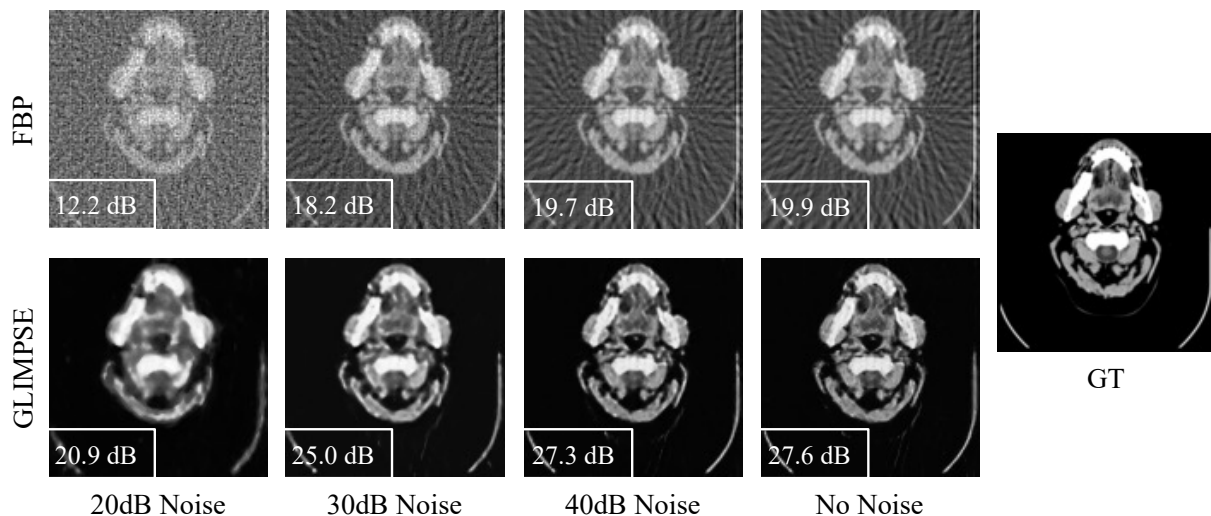
The proposed model comes with certain limitations. While the memory required by GLIMPSE hardly varies with image resolution, memory and computing costs increase as the number of projections r increases with the current MLP network. A promising alternative to the standard MLP architecture is the use of a mixture-of-experts layers [41]–[43], which selectively employ smaller MLPs for processing inputs. This mixture-of-experts approach is an effective drop-in replacement for standard MLP layers of language transformers [44] and vision transformers [26], as they increase the capacity of the layers without increasing the computational cost proportionally.

Moreover, while specifically designed for CT imaging, our localized architecture can integrate with various imaging problems involving line integrals in forward operators like photoacoustic [45], [46] and cryo-electron tomography (cryoET) [47]. In addition, although we introduced GLIMPSE specifically for 2D images, its adaptation to 3D shapes is a straightforward extension that can address the fundamental challenges for medical applications. This extension is particularly interesting given the ability of GLIMPSE to operate locally and its near-fixed memory requirement across resolution, which makes it an ideal choice for large 3D objects.

- [1] G. Wang, J. C. Ye, and B. De Man, “Deep learning for tomographic image reconstruction,” *Nature Machine Intelligence*, vol. 2, no. 12, pp. 737–748, 2020.
- [2] O. Ronneberger, P. Fischer, and T. Brox, “U-net: Convolutional networks for biomedical image segmentation,” in *Medical Image Computing and Computer-Assisted Intervention—MICCAI 2015: 18th International Conference, Munich, Germany, October 5–9, 2015, Proceedings, Part III 18*. Springer, 2015, pp. 234–241.
- [3] K. H. Jin, M. T. McCann, E. Froustey, and M. Unser, “Deep convolutional neural network for inverse problems in imaging,” *IEEE Transactions on Image Processing*, vol. 26, no. 9, pp. 4509–4522, 2017.
- [4] M. T. McCann, K. H. Jin, and M. Unser, “Convolutional neural networks for inverse problems in imaging: A review,” *IEEE Signal Processing Magazine*, vol. 34, no. 6, pp. 85–95, 2017.
- [5] N. Davoudi, X. L. Deán-Ben, and D. Razansky, “Deep learning photoacoustic tomography with sparse data,” *Nature Machine Intelligence*, vol. 1, no. 10, pp. 453–460, 2019.
- [6] T. Liu, A. Chaman, D. Belius, and I. Dokmanić, “Learning multiscale convolutional dictionaries for image reconstruction,” *IEEE Transactions on Computational Imaging*, vol. 8, pp. 425–437, 2022.
- [7] J. Adler and O. Öktem, “Solving ill-posed inverse problems using iterative deep neural networks,” *Inverse Problems*, vol. 33, no. 12, p. 124007, Nov 2017.
- [8] J. Adler and O. Öktem, “Learned primal-dual reconstruction,” *IEEE Transactions on Medical Imaging*, vol. 37, no. 6, pp. 1322–1332, 2018.
- [9] D. Gilton, G. Ongie, and R. Willett, “Neumann networks for linear inverse problems in imaging,” *IEEE Transactions on Computational Imaging*, vol. 6, pp. 328–343, 2019.
- [10] A. K. Maier, C. Syben, B. Stimpel, T. Würfl, M. Hoffmann, F. Schebesch, W. Fu, L. Mill, L. Kling, and S. Christiansen, “Learning with known operators reduces maximum error bounds,” *Nature machine intelligence*, vol. 1, no. 8, pp. 373–380, 2019.
- [11] A. Hauptmann, J. Adler, S. Arridge, and O. Öktem, “Multi-scale learned iterative reconstruction,” *IEEE Transactions on Computational Imaging*, vol. 6, pp. 843–856, 2020.
- [12] Y. B. Sahel, J. P. Bryan, B. Cleary, S. L. Farhi, and Y. C. Eldar, “Deep unrolled recovery in sparse biological imaging,” 2021.
- [13] J. Leuschner, M. Schmidt, P. S. Ganguly, V. Andriashen, S. B. Coban, A. Denker, D. Bauer, A. Hadjifaradji, K. J. Batenburg, P. Maass, and M. van Eijnatten, “Quantitative comparison of deep learning-based image reconstruction methods for low-dose and sparse-angle CT applications,” *Journal of Imaging*, vol. 7, no. 3, 2021.
- [14] L. A. Feldkamp, L. C. Davis, and J. W. Kress, “Practical cone-beam algorithm,” *Josa a*, vol. 1, no. 6, pp. 612–619, 1984.
- [15] H. K. Aggarwal, M. P. Mani, and M. Jacob, “Modl: Model-based deep learning architecture for inverse problems,” *IEEE transactions on medical imaging*, vol. 38, no. 2, pp. 394–405, 2018.
- [16] B. Hamoud, Y. Bahat, and T. Michaeli, “Beyond local processing: Adapting cnns for ct reconstruction,” in *European Conference on Computer Vision*. Springer, 2022, pp. 513–526.
- [17] A. Graas, S. B. Coban, K. J. Batenburg, and F. Lucka, “Just-in-time deep learning for real-time x-ray computed tomography,” *Scientific Reports*, vol. 13, no. 1, p. 20070, 2023.
- [18] A. H. Andersen and A. C. Kak, “Simultaneous algebraic reconstruction technique (sart): a superior implementation of the art algorithm,” *Ultrasonic imaging*, vol. 6, no. 1, pp. 81–94, 1984.
- [19] S. Lunz, A. Hauptmann, T. Tarvainen, C.-B. Schonlieb, and S. Arridge, “On learned operator correction in inverse problems,” *SIAM Journal on Imaging Sciences*, vol. 14, no. 1, pp. 92–127, 2021.
- [20] S. Gupta, K. Kothari, V. Debarnot, and I. Dokmanić, “Differentiable uncalibrated imaging,” *IEEE Transactions on Computational Imaging*, 2023.
- [21] E. Kang, J. Min, and J. C. Ye, “A deep convolutional neural network using directional wavelets for low-dose X-ray CT reconstruction,” *Medical physics*, vol. 44, no. 10, pp. e360–e375, 2017.
- [22] A. Khorashadizadeh, K. Kothari, L. Salsi, A. A. Harandi, M. de Hoop, and I. Dokmanić, “Conditional injective flows for bayesian imaging,” *IEEE Transactions on Computational Imaging*, vol. 9, pp. 224–237, 2023.
- [23] G. H. Golub and C. F. Van Loan, “An analysis of the total least squares problem,” *SIAM journal on numerical analysis*, vol. 17, no. 6, pp. 883–893, 1980.
- [24] I. Markovsky and S. Van Huffel, “Overview of total least-squares methods,” *Signal processing*, vol. 87, no. 10, pp. 2283–2302, 2007.



(a) In-distribution chest samples



(b) Out-of-distribution brain samples

Fig. 10: GLIMPSE performance on in-distribution and OOD data for different measurement noise levels.

- [25] S. Gupta and I. Dokmanić, "Total least squares phase retrieval," *IEEE Transactions on Signal Processing*, vol. 70, pp. 536–549, 2021.
- [26] A. Dosovitskiy, L. Beyer, A. Kolesnikov, D. Weissenborn, X. Zhai, T. Unterthiner, M. Dehghani, M. Minderer, G. Heigold, S. Gelly *et al.*, "An image is worth 16x16 words: Transformers for image recognition at scale," *arXiv preprint arXiv:2010.11929*, 2020.
- [27] I. O. Tolstikhin, N. Houlsby, A. Kolesnikov, L. Beyer, X. Zhai, T. Unterthiner, J. Yung, A. Steiner, D. Keysers, J. Uszkoreit *et al.*, "Mlp-mixer: An all-mlp architecture for vision," *Advances in neural information processing systems*, vol. 34, pp. 24 261–24 272, 2021.
- [28] Z. Pan, B. Zhuang, J. Liu, H. He, and J. Cai, "Scalable vision transformers with hierarchical pooling," in *Proceedings of the IEEE/cvf international conference on computer vision*, 2021, pp. 377–386.
- [29] Z. Wang, X. Cun, J. Bao, W. Zhou, J. Liu, and H. Li, "Uformer: A general u-shaped transformer for image restoration," in *Proceedings of the IEEE/CVF conference on computer vision and pattern recognition*, 2022, pp. 17 683–17 693.
- [30] G. Bachmann, S. Anagnostidis, and T. Hofmann, "Scaling mlps: A tale of inductive bias," *arXiv preprint arXiv:2306.13575*, 2023.
- [31] F. Altekürger, A. Denker, P. Hagemann, J. Hertrich, P. Maass, and G. Steidl, "Patchnr: Learning from small data by patch normalizing flow regularization," *arXiv preprint arXiv:2205.12021*, 2022.
- [32] A. Khorashadizadeh, A. Chaman, V. Debarnot, and I. Dokmanić, "Funknn: Neural interpolation for functional generation," in *ICLR*, 2023.
- [33] A. C. Kak and M. Slaney, *Principles of computerized tomographic imaging*. SIAM, 2001.
- [34] G. Wang, H. Yu, and B. De Man, "An outlook on x-ray ct research and development," *Medical physics*, vol. 35, no. 3, pp. 1051–1064, 2008.
- [35] L. De Chiffre, S. Carmignato, J.-P. Kruth, R. Schmitt, and A. Weckenmann, "Industrial applications of computed tomography," *CIRP annals*, vol. 63, no. 2, pp. 655–677, 2014.
- [36] K. Wells and D. Bradley, "A review of x-ray explosives detection techniques for checked baggage," *Applied Radiation and Isotopes*, vol. 70, no. 8, pp. 1729–1746, 2012.
- [37] A. Hauptmann and J. Poimala, "Model-corrected learned primal-dual models for fast limited-view photoacoustic tomography," *arXiv preprint arXiv:2304.01963*, 2023.
- [38] Z. Wang, A. C. Bovik, H. R. Sheikh, and E. P. Simoncelli, "Image quality assessment: from error visibility to structural similarity," *IEEE transactions on image processing*, vol. 13, no. 4, pp. 600–612, 2004.
- [39] J. Leuschner, M. Schmidt, D. O. Bagueer, and P. Maass, "Lodopab-ct, a benchmark dataset for low-dose computed tomography reconstruction," *Scientific Data*, vol. 8, no. 1, p. 109, 2021.
- [40] M. Hssayeni, M. Croock, A. Salman, H. Al-khafaji, Z. Yahya, and

- B. Ghorraani, “Computed tomography images for intracranial hemorrhage detection and segmentation,” *Intracranial Hemorrhage Segmentation Using A Deep Convolutional Model. Data*, vol. 5, no. 1, p. 14, 2020.
- [41] N. Shazeer, A. Mirhoseini, K. Maziarz, A. Davis, Q. Le, G. Hinton, and J. Dean, “Outrageously large neural networks: The sparsely-gated mixture-of-experts layer,” in *International Conference on Learning Representations*, 2017.
- [42] C. Riquelme, J. Puigcerver, B. Mustafa, M. Neumann, R. Jenatton, A. Susano Pinto, D. Keysers, and N. Houlsby, “Scaling vision with sparse mixture of experts,” *Advances in Neural Information Processing Systems*, vol. 34, pp. 8583–8595, 2021.
- [43] W. Fedus, J. Dean, and B. Zoph, “A review of sparse expert models in deep learning,” *arXiv preprint arXiv:2209.01667*, 2022.
- [44] A. Vaswani, N. Shazeer, N. Parmar, J. Uszkoreit, L. Jones, A. N. Gomez, Ł. Kaiser, and I. Polosukhin, “Attention is all you need,” *Advances in neural information processing systems*, vol. 30, 2017.
- [45] A. P. Jathoul, J. Laufer, O. Ogunlade, B. Treeby, B. Cox, E. Zhang, P. Johnson, A. R. Pizzey, B. Philip, T. Marafioti *et al.*, “Deep in vivo photoacoustic imaging of mammalian tissues using a tyrosinase-based genetic reporter,” *Nature Photonics*, vol. 9, no. 4, pp. 239–246, 2015.
- [46] J. Yao, L. Wang, J.-M. Yang, K. I. Maslov, T. T. Wong, L. Li, C.-H. Huang, J. Zou, and L. V. Wang, “High-speed label-free functional photoacoustic microscopy of mouse brain in action,” *Nature methods*, vol. 12, no. 5, pp. 407–410, 2015.
- [47] A. Doerr, “Cryo-electron tomography,” *Nature Methods*, vol. 14, no. 1, pp. 34–34, 2017.
- [48] A. Paszke, S. Gross, F. Massa, A. Lerer, J. Bradbury, G. Chanan, T. Killeen, Z. Lin, N. Gimelshein, L. Antiga *et al.*, “Pytorch: An imperative style, high-performance deep learning library,” *Advances in neural information processing systems*, vol. 32, 2019.
- [49] D. P. Kingma and J. Ba, “Adam: A method for stochastic optimization,” *arXiv preprint arXiv:1412.6980*, 2014.

Supplementary Information

S-1. NETWORK ARCHITECTURE AND TRAINING DETAILS

For GLIMPSE architecture, we use an MLP network comprising 9 hidden layers, each with dimensions [256, 256, 256, 256, 128, 128, 128, 64, 64] with ReLu activations. The input to the MLP network consists of sinusoidal curves sampled from $K = 9^2$ neighboring pixels. To prevent edge artifact of the circular convolution, we apply zero-padding with a size of 512 to the sinogram before applying the filter \mathbf{h} . Linear interpolation is used in (7). For the experiment in resolution 512×512 in Section IV-B, we use a larger network with hidden layer dimensions [1024, 1024, 1024, 512, 512, 512, 256, 256] to enhance the quality of reconstructions.

We implement our model in PyTorch [48] on a machine equipped with a Nvidia A100 GPU with 80GB of memory to train the different architectures. We report the maximum capacity of the graphics card during training and the time needed to complete the training. All models in Section IV were trained for 200 epochs with MSE loss using the Adam optimizer [49]. A learning rate 10^{-4} was used for GLIMPSE and U-Net, while LGS and LPD were trained with a learning rate 10^{-3} . All models were trained with batch size 64. In the case of GLIMPSE, for each mini-batch of random objects, we performed optimization on a random mini-batch of 512 pixels 3 times.

S-2. OPTIMAL FILTER FOR FBP RECONSTRUCTION

Proposition 2 (Reconstruction for continuous Radon transform). *We have the following identity*

$$f(x, y) = \int_0^\pi Rf(\theta, \cdot) \star \psi d\theta,$$

where ψ is the filter that has for Fourier transform $|\cdot|$.

Proof. Let $\mathbf{p} = (x, y)$, $\boldsymbol{\xi} = (\xi_1, \xi_2)$. We have

$$\begin{aligned} f(x, y) &= \int_{-\infty}^{+\infty} \int_{-\infty}^{+\infty} \mathcal{F}_{2D}(f)(\xi_1, \xi_2) \exp(2i\pi(\boldsymbol{\xi}, \mathbf{p})) d\boldsymbol{\xi} \\ &= \int_0^{+\infty} \int_0^{2\pi} \mathcal{F}_{2D}(f)(r \cos(\theta), r \sin(\theta)) \\ &\quad \exp(2i\pi r \langle \mathbf{k}, \mathbf{p} \rangle) r dr d\theta, \end{aligned}$$

by doing a change of variable in polar coordinates, where $\mathbf{k} = (\cos(\theta), \sin(\theta))$. Observe that $\mathcal{F}_{2D}(f)(r \cos(\theta), r \sin(\theta))$ is the Fourier Transform of f along the line of direction \mathbf{k} . By the Fourier slice theorem [33], we have

$$\mathcal{F}_{2D}(f)(r \cos(\theta), r \sin(\theta)) = \mathcal{F}_{1D}(Rf(\theta, \cdot))(r)$$

By symmetry of the Radon transform, we have $Rf(\theta, r) = Rf(\theta + \pi, -r)$. Finally,

$$\begin{aligned} f(x, y) &= \int_{-\infty}^{+\infty} \int_0^\pi \mathcal{F}_{1D}(Rf(\theta, \cdot))(r) \exp(2i\pi r \langle \mathbf{k}, \mathbf{p} \rangle) \\ &\quad |r| dr d\theta = \int_0^\pi \mathcal{F}_{1D}^{-1}(\mathcal{F}_{1D}(Rf(\theta, \cdot)) \odot |\cdot|) d\theta. \end{aligned}$$

This shows that

$$f(x, y) = \int_0^\pi (Rf(\theta, \cdot) \star \psi)(\langle \mathbf{k}, \mathbf{p} \rangle) d\theta,$$

where ψ is the filter that has for Fourier transform $|\cdot|$. \square

S-3. PROOF OF PROPOSITION 1

Proof. Using the definition of the radon transform in (2), we have

$$\begin{aligned} Rf(\alpha, t) &= \int_{-\infty}^{+\infty} \delta(z \cos(\alpha) - t \sin(\alpha) - x, \\ &\quad z \sin(\alpha) + t \cos(\alpha) - y) dz. \end{aligned}$$

Solving $z \cos(\alpha) - t \sin(\alpha) - x = 0$ for z leads to

$$z = \frac{t \sin(\alpha) + x}{\cos(\alpha)}.$$

Then, solving $z \sin(\alpha) + t \cos(\alpha) - y = 0$ for t , using the previous expression for z leads to

$$t = y \cos(\alpha) - x \sin(\alpha). \quad \square$$